Morphology Controlled Synthesis of Nanoporous Co_3O_4 Nanostructures and Their Charge Storage Characteristics in Supercapacitors

Kalyanjyoti Deori,[‡] Sanjeev Kumar Ujjain,[‡] Raj Kishore Sharma, and Sasanka Deka*

Department of Chemistry, University of Delhi, North Campus, Delhi 110007, India

⑤ *Supporting Information*

ABSTRACT: Cubic spinel Co_3O_4 nanoparticles with spherical (0D) and hexagonal platelet (2D) morphologies were synthesized using a simple solvothermal method by tuning the reaction time. XRD and HRTEM analyses revealed pure phase with growth of Co_3O_4 particles along [111] and [110] directions. UV−vis studies showed two clear optical absorption peaks corresponding to two optical band gaps in the range of 400−500 nm and 700−800 nm, respectively, related to the ligand to metal charge transfer events ($O^{2-} \rightarrow Co^{2+,3+}$). Under the electrochemical study in two electrode assembly system ($Co_3O_4/KOH/Co_3O_4$) without adding any large area support or a conductive filler, the hexagonal platelet Co_3O_4 particles exhibited comparatively better characteristics with high specific capacitance (476 F g^{-1}), energy density 42.3 Wh kg^{-1} and power density 1.56 kW kg^{-1} at current density of 0.5 Ag^{-1}, that suited for potential applications in supercapacitors. The observed better electrochemical properties of the nanoporous Co_3O_4 particles is attributed to the layered platelet structural arrangement of the hexagonal platelet and the presence of exceptionally high numbers of regularly ordered pores.

Co₃O₄ hexagonal platelet
Specific capacitance= 476 Fg⁻¹
Energy density= 42.3 Wh kg⁻¹
Power density= 1.56 kW kg⁻¹

KEYWORDS: *2D nanocrystals, cobalt oxide, pseudocapacitor, nanoporous, charge storage*
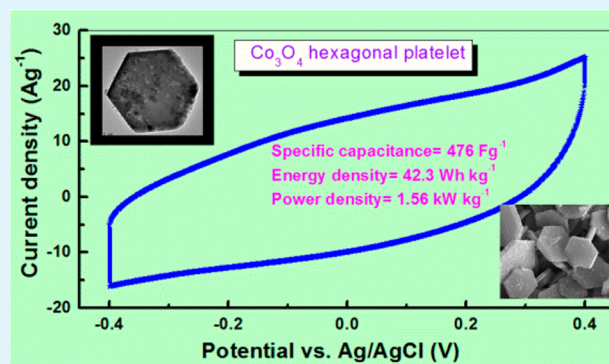
1. INTRODUCTION

The control over the morphology of nanocrystals with well-defined shape and uniform size remains an important goal of modern synthetic chemistry, because shape- and size-controlled nanocrystals are promising candidates as active components in a wide range of technological applications, and are model system for basic research. On this basis, much attention has been paid to synthesize monodispersed nanocrystals with novel shapes which guarantees attractive physical and chemical properties.[1,2] In recent times, significant advances have been made in the production of nanocrystalline metal-oxide through the use of a variety of physical and chemical processes, because of its wide range of applications. Among those oxides, cobalt oxides (Co_3O_4) either in bulk or nanocrystalline form are extremely important functional materials towards electrochemical, magnetic, and catalytic application, for instance, supercapacitors,[3−5] various sensors,[6−8] CO oxidation,[9] H_2 gas generation,[10] heterogeneous catalysis for NO decomposition,[11] methane combustion,[12] oxidation of trace ethylene,[13] etc., because of their exceptional chemical and physical properties. Numerous methodologies have been developed to synthesize size and shape selective formation of CoO nanostructures, however, very few reports are available on the synthesis of morphology oriented Co_3O_4 nanostructures and their applications their off so far. Few of the novel developments

on Co_3O_4 nanostructures are quasi-single-crystalline Co_3O_4 nanowire arrays,[14] Co and Co_3O_4 nanoparticles by solid-state oxidation of a metallic colloid precursor,[15] nanocubes,[16] nanocages,[17] mesoporous nanostructures,[18] and recent report on air oxidation of fcc-CoO and hcp-CoO shape oriented nanocrystals to spinel-Co_3O_4.[19] Although uniform size and interesting shapes of these cobalt oxide nanoparticles have been investigated in recent years, but still development in this field is going on, particularly on control over novel morphologies and improved properties. This objective is challenging because single phase of cobalt oxide (either Co_3O_4 or CoO) is difficult to obtain in pure form by simple methods, often being contaminated with the other phase of cobalt oxide and/or Co metal. Furthermore, the constancy of the new synthesis method and applications of the as-synthesized cobalt oxide nanocrystals obtained selectively needs to be investigated in detail.

Co_3O_4 could be a good example of pseudocapacitors along with other established materials,[20,21] in which charge is stored using redox-based Faradic reactions, can have higher capacitance values than electric double layer capacitors (EDLCs) and can have higher power densities than that of

secondary batteries.[22−25] Co_3O_4 based pseudocapacitor devices which are alternate energy storage devices, are important in pulsed power applications such as in hybrid electric vehicles, memory back-up, military and space equipment, wearable electronics, paperlike electronics, flexible biomedical devices, and day-to-day electronic devices.[26−29] The reason behind choosing Co_3O_4 as a promising candidate of pseudocapacitors over most promising hydrous RuO_2 is cost, toxicity effect, and the earlier one can provide a variety of oxidation states for efficient redox charge transfer.[30,31]

In addition, spinel Co_3O_4 is environmentally friendly and has high theoretical capacitance (3560 F/g). Very recently Rakhi et al. reported an expectedly high specific capacitance ∼1500 F/g upon increasing the electrochemically active surface of Co_3O_4.[32] Wu et al. and Wang et al. independently reported that electron and ion transport efficiency for charge storage in Co_3O_4 based pseudocapacitors mainly depends on properties such as surface area, morphology, and specific orientation of different facets.[33,34] However, there are few other reports also available on the pseudocapacitance value ranging from 200 to 1400 F/g at a current density of 0.1−0.3 A/g of Co_3O_4 nanostructures. But in most of the cases, the nanostructures have been deposited or grown on Ni-foam or carbon-substrates. The widely studied Co_3O_4 nanostructure is mainly 1D, for instance nanowires, nanorods and nanotubes.[32,35−37] Eventhough, a wide variety of microstructures and morphologies composed of 1D and 3D nanostructures have been synthesized and tested for capacitance study, it still a great challenge to identify a promising 2D nanostructure that has enhanced charge storage capacity and cycling life relative to other reported specific capacitance of Co_3O_4. To the best of our knowledge, no report is available on effect of variation in morphology from 0D to 2D, studies on the capacitive performance and finally correlation of the pseudocapacitance of Co_3O_4 nanostructures with surface area and exposed facets.

Herein we demonstrate a simple solvothermal strategy to synthesize very stable monodispersed Co_3O_4 nanocrystals with spherical (0D) and hexagonal platelet (2D) morphologies depending on the control over reaction time. Our method is a direct synthesis method of Co_3O_4 via the production of β-$Co(OH)_2$ as an intermediate. The sizes of as prepared Co_3O_4 nanospheres were found to be in 30−35 nm range and the hexagonal platelets are 3−4 μm in diameter and ∼100 nm in thickness. Further, the optical properties of the obtained Co_3O_4 particles were studied via a UV−visible spectrophotometer. Interestingly two distinct optical band gaps were observed for both morphologies of Co_3O_4 in their absorption spectra. Electrochemical performance of the synthesized materials was evaluated using Cyclic voltammetry (CV), electrochemical impedance spectroscopy (EIS) and galvanostatic charge-discharge (GCD) in two electrode cell assembly (Co_3O_4/KOH/Co_3O_4). The results for the Co_3O_4 hexagonal platelet are only presented because of its highest capacitance compared to β-$Co(OH)_2$, CoO, and spherical Co_3O_4 nanoparticles. In the present work, we have obtained ∼476 F/g specific capacitance with very high energy and power density of 42.3 Wh kg^{-1} and 1.56 kW kg^{-1} respectively at a high current density of 0.5 A g^{-1} without utilizing any large area support. This suggest that the present Co_3O_4 is an improved metal oxide and exhibit better performance compared to other metal oxides like MnO_2, TiO_2, SnO_2, etc. and can be utilized for supercapacitor device fabrication. The overall electrochemical values and performance of our hexagonal Co_3O_4 platelet particles as pseudocapacitive

material are excellent over most of the other reported Co_3O_4 micro/nanostructures.[38−40]

2. EXPERIMENTAL SECTION

2.1. Materials. Cobalt acetate ($Co(CH_3COO)_2·4H_2O$, 99%, Thomas Baker), absolute ethanol (C_2H_5OH, 99.9%, Changshu Yangyuan chemical, China), NaOH (98%, Merck-India), cationic surfactant cetyl tri-methyl ammonium bromide (CTAB, 99%, SRL-India), nonionic surfactants polyethylene glycol (PEG-400) (Merck, India) and Triton X-100 (SRL, India). All chemicals were used as received without further purification.

2.2. Synthesis of Co_3O_4 Hexagonal Platelet and Sphere. Here we have carried out two syntheses. In the first synthesis, cobalt acetate (1 mmol) was dissolved in 40 mL of ethanol and then 5 mL of aqueous NaOH solution (0.04 N) was added under vigorous stirring, during which brown precipitate appeared. The reaction mixture was then transferred to a stainless steel solvothermal reaction autoclave vessel with Teflon lining and maintained the vessel at 220 °C for 20 h in a PID controlled oven with controlled heating rate and then cooled to room temperature naturally. This reaction was carried out without the addition of any surfactant. In the second synthesis, all reaction parameters have been kept constant as mentioned above, except the solvothermal reaction time was increased to 36 h instead of 20 h. Note that this reaction was also carried out without the addition of any surfactant. Upon cooling to room temperature, the as-obtained black precipitate was centrifuged and washed with distilled water and absolute ethanol for three times. The precipitate was either redispersed in suitable solvents (such as ethanol or water) or dried at 40 °C for 4 h in air if various characterizations had to be carried out on it. The product obtained in the 20 h reaction is labeled as sample20 and the product from the 36 h reaction is labeled as sample36. Annealing of the as-synthesized sample20 and sample36 for further studies have been performed at 300 °C for 3 h in air in a muffle furnace.

2.3. Characterization. *Transmission Electron Microscopy (TEM).* Samples for TEM were prepared by dropping nanocrystal dispersion in suitable solvent onto carbon coated copper grids and letting the solvent evaporate at room temperature. Low resolution TEM images, Phase-contrast high-resolution TEM (HRTEM), selected area electron diffraction (SAED), and energy dispersive spectrometry (EDAX) measurements were performed with a Philips Technai G^{2}30 transmission electron microscope operating at an accelerating voltage of 300 kV and equipped with energy dispersive spectrometry (EDAX).

Powder X-ray Diffraction (XRD). XRD measurements were performed with a Bruker D8 Advance X- ray diffractometer employing monochromatized Cu Kα radiation (λ = 1.54056 Å) at 298 K. Dry powder was spread on top of a glass substrate and was then measured in reflection geometry.

Scanning Electron Microscopy (SEM). SEM measurements for morphological characterization of the particles were done on a ZEISS oxford instrument EV0, MA15 equipped with energy dispersive spectrometry (EDS). Thick concentrated sample solution was first drop casted on an ultrasonically cleaned ITO substrate letting the solvent evaporate.

Thermal Analysis (TGA/DSC). The thermogravimetric and differential scanning calorimetric (TG/DSC) analyses were carried out on a Perkin-Elmer Diamond TG/DTA Instruments in air atmosphere from ambient temperature 25 to 800 °C at a heating rate of 5 °C/min with a sample mass of 2.248 mg in an aluminum pan.

UV−vis Absorption Spectroscopy. Absorption measurements were carried out on a Perkin-Elmer Lambda 35 spectrophotometer. Nearly clear dispersion of the sample in ethanol was prepared by ultrasonication for the purpose.

Surface Area and Pore Size. Surface area of samples were determined by Brunauer-Emmett-Teller (BET) principle and the pore parameters of the samples were determined by Barrett−Joyner−Halenda (BJH) method using 20 points BET equation with the help of Quantachrome instruments (Model NOVA 2000e surface area and pore size analyzer) at 77 K.
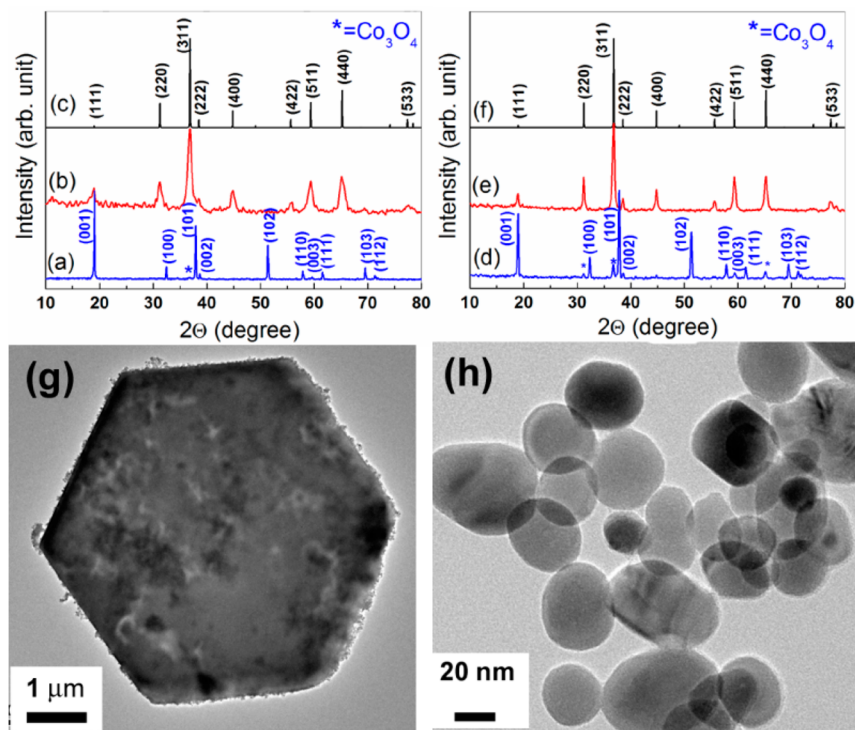
Figure 1. Powder XRD pattern of (a) as-prepared sample20, (b) after annealing sample20, (c) bulk Co_3O_4, (d) as-prepared sample36, (e) after annealing sample36, (f) bulk Co_3O_4. (g) Low-magnification TEM image of as-synthesized sample20 (more images in Figure S3 in the Supporting Information) and (h) low-magnification TEM image of as-synthesized sample36.

2.4. Electrochemical Analysis. Preparation of electrode: Finely ground Co_3O_4 powder was taken in a solution of 5 wt % nafion in iso-propyl alcohol (IPA) and mixed ultrasonically for 30 min. So obtained suspension was sprayed onto the polished graphite plates. These spray deposited thin films were dried at 80 °C overnight and used as working electrodes. Cyclic Voltammetry (CV), electrochemical impedance spectroscopy (EIS) and galvanostatic charge-discharge (GCD) for cell assembly ($Co_3O_4/KOH/Co_3O_4$) of supercapacitors were performed on a two electrode cell with a mass loading of 0.9 mg/cm^2 on single electrode. CV and EIS measurements were performed using an electrochemical analyzer (Model: CHI 604 D, CH Instruments, USA). Galvanostatic charge−discharge was recorded at different current densities using charge−discharge unit (model: BT 2000, Arbin Instruments, USA).

2 M aqueous KOH solution served as electrolyte and Nafion 115 membrane was employed as the separator. The CV and GCD measurements were performed in a potential window −0.4 to +0.4 V. EIS measurement was conducted in a frequency range from 0.01 Hz to 100 kHz. The specific capacitance was calculated from the galvanostatic charge−discharge curves according to Wu et al.[41] using following equations

$$C = \frac{I}{\nu m} \qquad (1)$$

where I is the current, ν is scan rate, and m is the mass loading on electrode. Alternatively, specific capacitance was calculated from galvanostatic charge discharge curve according to the following equation

$$C = \frac{I\Delta t}{m\Delta V} \qquad (2)$$

where $\Delta V/\Delta t$ is the change in potential with time t. The energy density (E in Wh kg^{-1}) and power density (P in kW kg^{-1}) were expressed as

$$E = \frac{1}{2 \times 3.6} CV^2 \qquad (3)$$

$$P = \frac{V^2}{4mR} \qquad (4)$$

where C is the measured device capacitance, V is the operating voltage window, and R is the equivalent series resistance calculated from IR drop in galvanostatic discharge curve.

3. RESULTS AND DISCUSSION

3.1. Phase Purity and Influence of Reaction Time on the Morphology of Co_3O_4 Nanoparticles. The structural-composition details of the products obtained from the two syntheses carried out without the addition of any surfactants for 20 h and 36 h reaction time keeping the other parameters constant have been studied by powder XRD analyses. Interestingly, rather matching with standard Co_3O_4 pattern, the experimental XRD patterns of as-synthesized sample20 and sample36 matched with hexagonal phase cobalt hydroxide β-$Co(OH)_2$ (JCPDS card #30-443). The normalized powder XRD patterns of the as-synthesized products are shown in Figure 1 (XRD pattern a and d) along with bulk XRD pattern of Co_3O_4 (JCPDS card #42-1467). To examine the morphology of these β-$Co(OH)_2$ samples, we have carried out low-resolution TEM imaging and the results are shown in lower panel of Figure 1. Interestingly particles of two different morphologies with separate sizes have been obtained for the two samples. Big hexagonal platelets (2D) with average diameter 3−4 μm (edge to edge) and thickness of ∼100 nm are seen for Sample20 (Figure 1g). However, the as-synthesized sample36 is small in diameter and spherical (0D) in morphology (Figure 1h). The average particle diameter of these spherical particles is 30 nm. A longer reaction time favors the formation of thermodynamically more stable shape, which is spherical in the present case. The radius difference (δr/r, at

20h and 36h) reduces as growth proceeds and finally become zero (0), i.e., the formation of consistent spherical particles.

To see the effect of varying reaction time (10-36 h, without the addition of surfactants) and addition of hydrolytic surfactants, we have further carried out several control syntheses reactions and based on these a growth mechanism for the reported particles has been proposed. Initially we have carried out control syntheses by adding surfactants such as CTAB, Triton X-100 and PEG-400 to our reported reactions to improve the size and morphology keeping the other parameters constant. However, we have ended up with mixed phases of CoO, Co_3O_4 and β-Co(OH)$_2$ and mixed morphologies such as nanorods, cubes, spheres, triangles, etc. (See Table S1 and Figure S1 in the Supporting Information for details). Thereafter, solvothermal reactions have been carried out for 10 h and 30 h without the addition of any surfactant. When we closely examined 10 h reaction data as shown in Figure S2d in the Supporting Information, mainly sheetlike and hexagonal/ trianglelike morphologies with average diameter 100−200 nm of pure hexagonal β-Co(OH)$_2$ were found. It may be noted that these sheetlike nanoparticles were further grown by a nucleation−dissolution−recrystallization growth mechanism and uniformly arranged to make hexagonal platelet particles after completion of 20 h of reaction time. In the process, these kinetically stable microparticles were broken down to smaller particles of β-Co(OH)$_2$ in further increase of reaction time, i.e., at 30 h, as shown in Figure S2e in the Supporting Information. The reason of breakdown of microparticle is not known at present. Finally, only spherical particles were obtained for the 36 h reaction as shown in Figure 1h. Therefore, it can be stated that at the end of 36 h reaction, thermodynamically stable uniform spherical nanoparticles were formed.

It is reported that β-Co(OH)$_2$ can be oxidized to Co_3O_4 at elevated temperature.[12] To know the exact temperature at which our as-synthesized β-Co(OH)$_2$ intermediate nanoparticles could be converted to Co_3O_4, thermo-gravimetric analysis (TGA) has been carried out on these samples. A combined TGA/DSC curve of sample20 is shown in Figure 2. The major weight loss in a single step (thick line, 17.18%) was observed over the temperature range 200−400 °C, which is due to the dehydroxylation of the compound according to the following reaction
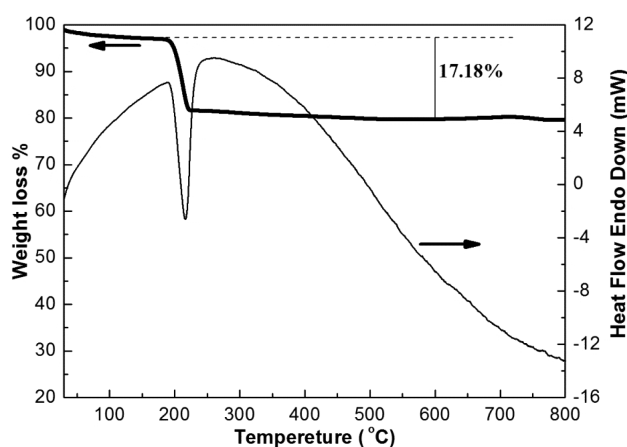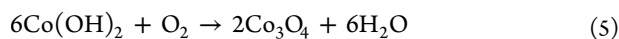
$$6Co(OH)_2 + O_2 \rightarrow 2Co_3O_4 + 6H_2O \qquad (5)$$

Figure 2. Combined TGA/DSC curve of the as-prepared intermediate β-Co(OH)$_2$ sample.

An endothermic peak appeared in the corresponding region in the derivative scanning calorimetric (DSC, thin line) curve, which indicated a transformation of β-Co(OH)$_2$ to Co_3O_4. To clarify the exact role of post heating treatment, we annealed our β-Co(OH)$_2$ samples at 300°C for 3 h and the XRD patterns of the annealed sample20 and sample36 are compared in Figure 1 (XRD pattern b and e). An absolved phase transformation could be revealed from the comparison of the XRD patterns, where all the peaks of β-Co(OH)$_2$ disappeared and new peaks appeared after annealing located at 2θ = 18.91, 31.15, 36.84, 38.47, 44.78, 55.64, 59.30, and 65.11°, which correspond to (111), (220), (311), (222), (400), (422), (511), and (440) planes, respectively, of cubic spinel Co_3O_4 ($Fd3m$, a = 8.083 Å, JCPDS #42-1467). No shift in the peak position is measured between the experimental and bulk XRD patterns in the whole 2θ range (10−80°), indicating that the produced cubic Co_3O_4 NCs do not have any additional strain. After detailed structural characterization from X-ray diffraction pattern (from the least-squares refinement of the XRD patterns using the PowderCell program)[42] it can be concluded that the as-synthesized material is crystalline pure cubic phase Co_3O_4 with calculated cell parameter a = 8.081 Å, and space group $Fd3m$. No other phases, such as CoO (JCPDS #78-0431) or β-Co(OH)$_2$ were detected in the XRD pattern confirming the high purity of the annealed products. Moreover, no peak broadening or sharpening is observed in the annealed samples indicating the retainment of the average crystallite size constant (see Figure S4 in the Supporting Information). Thereafter, we use sample20 and sample36 code for the annealed hexagonal platelet and spherical samples, respectively.

Further, structural-compositional and morphology details of the annealed samples have been studied by combined TEM/ HRTEM and SEM analyses. Representative results are illustrated in Figure 3. TEM image in Figure 3a shows that the hexagonal platelet shape of the as-synthesized β-Co(OH)$_2$ from sample20 does not get changed upon heating and the final Co_3O_4 particles remain similar in morphology. Equal size distribution of the hexagonal platelets can be seen in the SEM image in Figure 3b. The average diameter (edge-to-edge) and thickness of these platelets are 3−4 μm and ~100 nm, respectively, which is rather large as compared to sample36. Phase identification was made from scaled SAED images from a region of the Co_3O_4 hexagonal particles by calculating the lattice spacing and then comparing with standard JCPDS values (#42-1467) as shown in Figure 3c. The observed spotty SAED pattern reveal the pure crystalline nature of the annealed particles with cubic crystal structure, where (111), (220), (400), and (311) lattice planes were clearly indexed in agreement with XRD data. However, spotty rings were observed due to random orientations of single-crystalline Co_3O_4 in the TEM grid in different directions. Similar for sample36, the annealed sample is again remains spherical in shape and the average particle diameter is 25−30 nm (Figure 3d). Images e and f in Figure 3 show phase contrast high resolution transmission electron micrographs (HRTEM) from two different Co_3O_4 nanocrystallites. Figure 3e images the 0.45 nm spaced lattice fringes correspond to (111) plane of cubic Co_3O_4. However, in the case of the second particle, we see distinctive sets of fringes which can be unambiguously identified, such as those corresponding to (220) planes of bulk fcc-Co_3O_4 (d_{220}^{Co3O4} = 0.28 nm) and (111) plans of Co_3O_4 (d_{111}^{Co3O4} = 0.45 nm). The clear lattice fringes from the phase-contrast HRTEM image indicated that the annealed
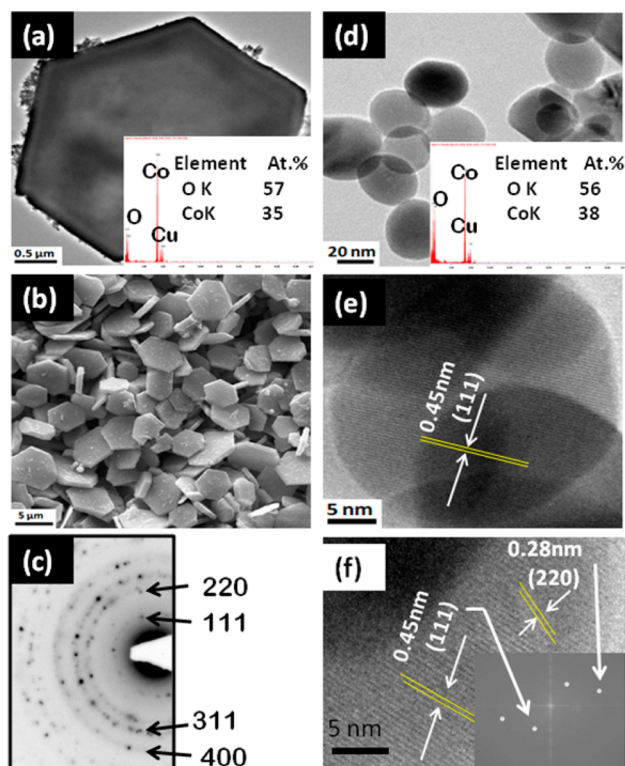
Figure 3. (a) Low-magnification TEM image (inset: EDAX analysis), (b) SEM image, and (c) SAED analysis of annealed sample20. (d) Low-magnification TEM image (inset: EDAX analysis), (e) representative phase contrast HRTEM image of an annealed sample36 single particle, and (f) phase contrast HRTEM image of another annealed sample36 single particle where lattice fringes of two different planes are observed. The inset in f shows their two-dimensional fast Fourier transform (2D-FFT) calculated from panel f. FFTs are marked by white dots for clarity.

Co_3O_4 sample36 was free from dislocations and stacking faults and it is single crystalline in nature. Two-dimensional fast fourier transform (2D-FFT) pattern calculated from the Co_3O_4 section seen in panel f is shown as inset in Figure 3f. This also confirms the presence of high-energy (220) planes or growth of Co_3O_4 particles in both [111] and [110] directions. Furthermore, elemental analysis was done using TEM-EDAX and the results are shown as inset in panels a and d in Figure 3 for those corresponding annealed samples. Co:O ratio was found to be near to 3:4 for both the samples. Thus from the TGA/DSC, annealing, XRD and HRTEM analyses of post annealing samples, we are confirmed that the annealed hexagonal platelet and spherical particles are of single-crystalline Co_3O_4 which are exposed in both {111} and {110} facets.

3.2. Optical Absorption and Surface Area Studies. The optical properties of the Co_3O_4 nanocrystals have been studied by room temperature UV−visible (UV−vis) absorption spectroscopy on the dispersed solution in ethanol to further assess their quality. Representative UV−vis spectra (Figure 4a) of both the samples show distinct absorptions at two different positions, centered at 430 nm and 750 nm for sample20 and at 400 nm and 755 nm for sample36, respectively. The observed two distinct absorption peaks at different wavelength λ for both the samples could be assigned to ligand to metal charge transfer (LMCT) events, such as, $O^{2-} \rightarrow Co^{2+}$ for the first absorption ($\lambda < 500$ nm) and $O^{2-} \rightarrow Co^{3+}$ for the second absorption ($\lambda >$
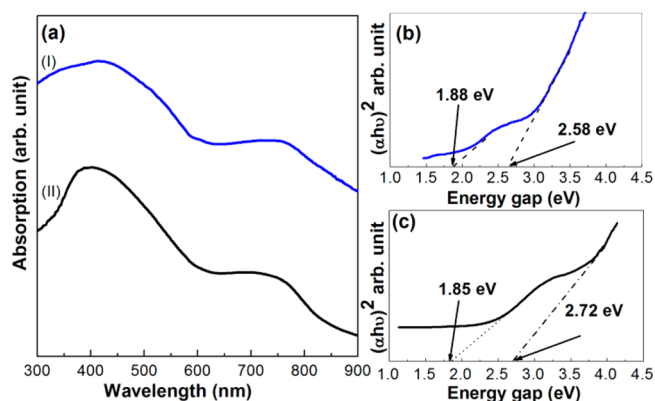

Figure 4. (a) Optical absorption spectra of Co_3O_4 (I) for hexagonal platelets and (II) for spherical nanoparticles, (b, c) corresponding band gaps, which were evaluated from the plot of $(AE_{Photon})^2$ vs E_{Photon}.

700 nm) respectively.[43] The band gap was calculated by taking the approximation of $(Ah\nu)^n$ versus $h\nu$ (where A is the optical density and $h\nu$ is the photon energy). The plot of $(Ah\nu)^n$ vs. $h\nu$ is drawn for the allowed direct band gap ($n = 2$) and indirect band gap ($n = 1/2$) and at first a band gap E_g of 1.88 eV and 2.58 eV for sample20 and 1.85 eV and 2.72 eV for sample36 were determined from the extrapolated intercept with the energy ($h\nu$) axis as shown in panels b and c in Figure 4, respectively. Further the optical band gap energy difference ($\Delta E = E_{g1} - E_{g2}$) was calculated for both the samples and the differences were found to be 0.7 eV for sample20 and 0.87 eV for sample36, respectively, which are in good agreement with the reported values for Co_3O_4.[43−45] The band gap energy difference is little higher in the case of spherical particles (sample36) than hexagonal one (sample20) because of the small-sized particles and quantum confinement effect.

Because the aim of the present work is to establish our hexagonal platelet Co_3O_4 nanocrystals as good example of supercapacitor material, we have carried out detailed N_2 adsorption−desorption study to find out available surface as well as the pore size and pore volume which is important for the pseudocapacitor behavior and double layer capacitor behavior. Figure 5 shows the N_2 adsorption−desorption isotherm of Co_3O_4 hexagonal platelet sample. The N_2 isotherm of the sample is of type IV and the hysteresis is the combination of type H2 and type H3, typical of a mesoporous sample[35] but with few microporous samples. Specific surface area was determined from the BET plots using the multipoint BET equation. Very high surface areas of magnitude 289 m^2/g were recorded for this sample. This surprising very high value of surface area for micrometer size particle is interesting in the present case. Generally surface area <10 m^2/g is expected for a bulk particle. The observed surface area is attributed to two reasons: (i) the anisotropic shape of the particles, as both opposite side surfaces and 6 adjacent edges contributed to the total surface area and (ii) high porosity. To relate the high porosity and observed high surface area, we have performed the pore-radius vs. their distribution measurement. The pore-size distribution curves calculated from the Barrett−Joyner−Halenda (BJH) method indicated the presence of micro- and mesoporosity, although they evidence the presence of regularly ordered pores (see inset in Figure 5). A maximum pore distribution was observed at around 1-4 nm. The formation of observed pores could be due to the removal of H_2O molecules[4] (as shown in reaction 5) during the phase transformation of β-
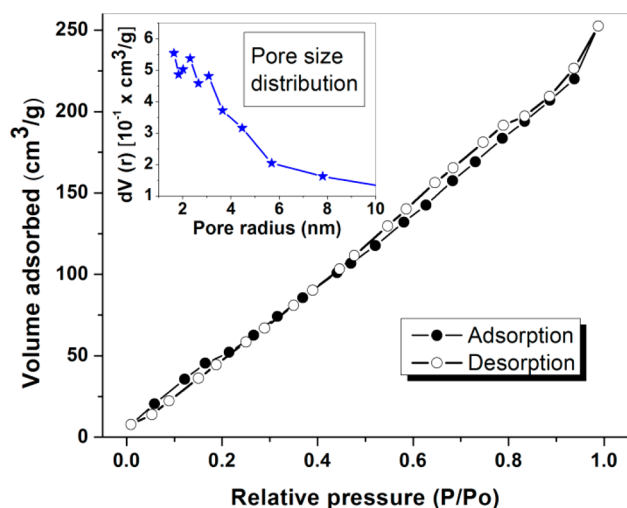
Figure 5. N_2 adsorption/desorption isotherm of Co_3O_4 hexagonal platelet sample at 77 K. Inset: Pore volume distribution vs. pore radius of the annealed hexagonal platelet particles.

$Co(OH)_2$ hexagonal platelet to Co_3O_4 keeping the original morphology intact. As it is known that a very large surface area and high micro/nanoporosity is always associated with large capacitance value,[46] vice versa, in the present case, we can expect a large capacitance value, and the observed high surface area is due to the presence of pores. It is important to mention here that, we have tried to detect the pores with the help of HRTEM, but could not succeed because of the thickness of the platelet sample. The origin of pseudocapacitance in electroactive materials like Co_3O_4 is the interfacial redox reactions, which strongly depends on the grain size, morphology, and porosity-dependent proton transfer. Thus larger intercalating anions induce higher porosity, which is proportional to capacitance.[46]

3.3. Electrochemical Study. To examine the electrochemical behavior, Cyclic Voltammetric (CV) measurements shown in Figure 6a have been carried out in a three-electrode system at a scan rate of 50 mV s^{-1} employing the as-synthesized β-$Co(OH)_2$ particles, annealed hexagonal platelet Co_3O_4 particles, and a separately prepared CoO nanoparticles sample from controlled synthesis (cubic, 30 nm, see the Supporting Information for XRD and BET) in 2 M KOH at a potential sweep window of -0.4 to +0.4 V. The shape of curves is slightly deviated from ideal rectangular voltammogram indicating pseudocapacitive behavior of cobalt oxides.[47] As seen in the voltammograms, hexagonal platelet Co_3O_4 particle covers large area on the applied voltage and output current scale, indicating the high charge storage among the three cobalt samples. A comparative electrochemical investigation of Co_3O_4 hexagonal platelet and spherical morphology is shown in Figure 6b. Co_3O_4 hexagonal platelets showed better capacitive performance over the spherical particles because of the existence of micropores in the layered morphology. Scan rate dependent voltammograms for Co_3O_4 hexagonal platelets shown in Figure 6c demonstrates excellent rate capability with more than 65% capacitive retention on going from 5 to 100 mV s^{-1}. Comparative scan rate dependence shown for all four Cobalt oxide/hydroxide particles in Figure 6d has also proved hexagonal platelets morphology of Co_3O_4 better pseudocapacitive material than others considered in the present study. Scan-rate-dependent CV curves of β-$Co(OH)_2$, cubic CoO
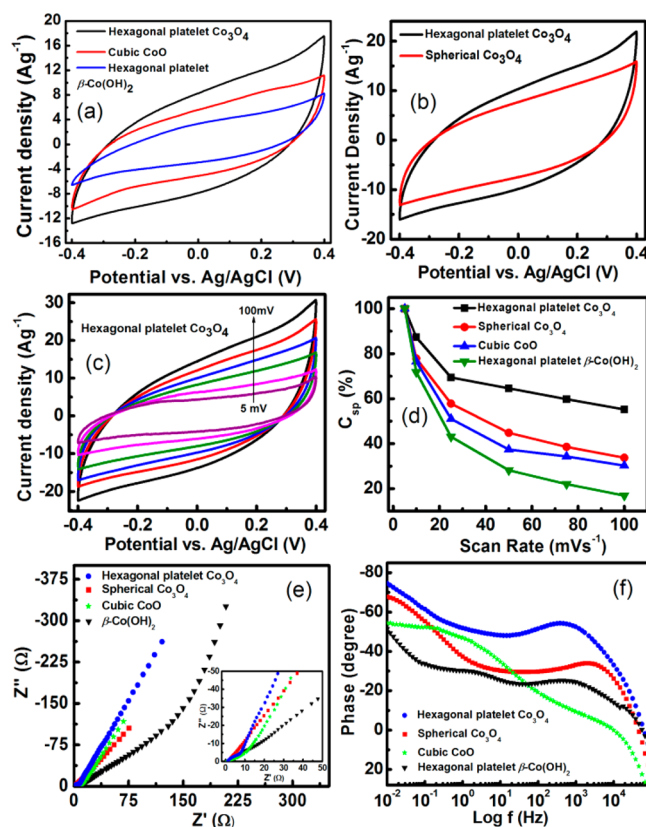

Figure 6. (a) Cyclic voltammograms (CV) of hexagonal platelet Co_3O_4, β-$Co(OH)_2$, and cubic CoO at 50 mV/s in three electrode system, (b) CV recorded for Co_3O_4 hexagonal platelets and spherical morphology, (c) CV for Co_3O_4 hexagonal platelets at different scan rates (5, 10, 25, 50, 75, and 100 mV/s), (d) comparative scan rate dependence curves of cobalt oxide/hydroxide samples, (e) Nyquist plot of cobalt oxide/hydroxide samples, the inset shows the zoom-in of Nyquist plot, and (f) Bode plot for all four cobalt oxide/hydroxide samples.

nanoparticles, and annealed spherical Co_3O_4 are shown in Figure S6 in the Supporting Information.

The electrochemical performance of the electrodes under discussion was further investigated by the electrochemical impedance spectroscopy (EIS) measurements. Figure 6e shows the Nyquist plots of all the electrodes in discussion. The ESR (equivalent series resistance) derived from the intersection of the Nyquist plot at the real axis in high frequency region is similar in all cases (shown in inset) but an increase in diameter of the semicircle (indicative of charge transfer resistance R_{ct}) from spherical Co_3O_4 to hexagonal β-$Co(OH)_2$ shape was observed. Spherical and platelet structure of Co_3O_4 as well as cubic CoO showed much smaller R_{ct} than β-$Co(OH)_2$ electrode (108 Ω). Although spherical and platelet structure Co_3O_4 as well as cubic CoO reveal similar R_{ct} but the hexagonal platelets of Co_3O_4 show high capacitive character in the low frequency region, which is also reflected in their Bode plot shown in Figure 6f. The hexagonal platelet Co_3O_4 showed maximum phase angle 78°, proved to demonstrate high supercapacitor characteristics compared to others cobalt oxides and hydroxide in the study.

On the basis of the above mentioned preliminary results, we consider the Co_3O_4 hexagonal platelet particles in this report to analyze in a supercapacitor device using CV & GCD measurements. The two-electrode (supercapacitor) geometry

is suggested in recent report to be better than the three-electrode configuration as the former mimics the physical configuration, internal voltages, and charge transfer that occurs in a supercapacitor cell and thereby providing the best indication of an electrode material's device performance.[48]

Figure 7a represents scan rate dependence on the hexagonal platelet Co_3O_4 voltammograms in two electrode system. The
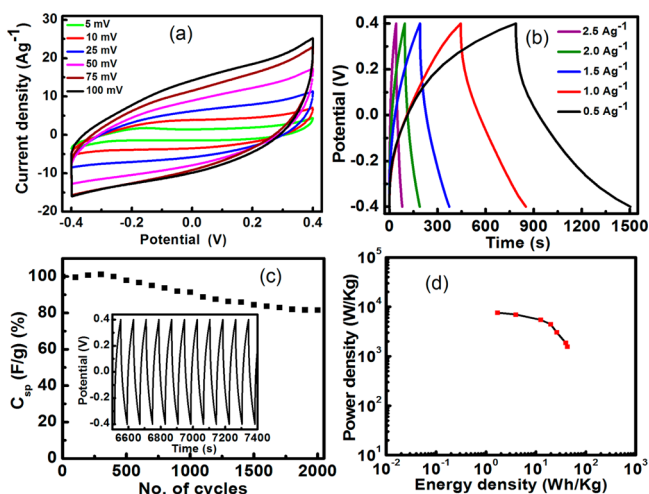

Figure 7. (a) Cyclic voltammograms (CV) recorded for Co_3O_4 hexagonal platelets in two electrode system at 5, 10, 25, 50, 75, and 100 mV/s, (b) charge-discharge curves of the Co_3O_4 two electrode cell at different current densities (0.5, 1.0, 1.5, 2.0, and 2.5 Ag^{-1}), (c) long-term cycling stability of the Co_3O_4 two electrode cell upon charge-discharge at a current density of 2.5 Ag^{-1}, and (d) Ragone plot of the Co_3O_4 supercapacitor. The energy density and power density were calculated from the charge−discharge curves at various current densities.

voltammograms are close to rectangular shape even at higher scan rate, which is an important characteristic in supercapacitors indicating high rate capability, low ESR, and thus a fast charging and discharging of the device. Each curve is composed of a capacitive current. This indicates that the electrodes are charged and discharged at a pseudoconstant rate over the complete voltammetric cycle.[32] The redox processes corresponding to the conversion between different cobalt oxidation states can be described by two sequential reactions[32]

$$Co_3O_4 + H_2O + OH^- \Leftrightarrow 3CoOOH + e^- \qquad (6)$$

$$CoOOH + OH^- \Leftrightarrow CoO_2 + H_2O + e^- \qquad (7)$$
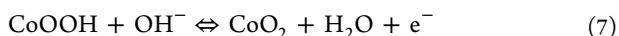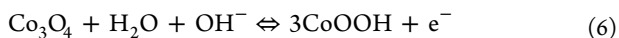
Nyquist plot of Co_3O_4 cell (see Figure S7 in the Supporting Information) exhibits almost vertical line in the low-frequency region, indicating that Co_3O_4 hexagonal platelet has high capacitive character. The cell demonstrates negligibly small (0.7 Ω) ESR with a charge transfer resistance (R_{CT}) of 2.8 Ω (knee frequency at 380 Hz). The small R_S and R_{CT} may be attributed to the regularly ordered mesoporosity in Co_3O_4 particles resulting high surface area and the platelet structure, which minimized the interfacial resistance of the charge transfer process.[4]

Figure 7b depicts the galvanostatic charge−discharge behavior of the two electrode cell of Co_3O_4 at different current densities in a potential window of −0.4 to +0.4 V. Its shape is slightly deviated from the typical triangular symmetric behavior indicating dominating pseudocapacitive contribution from

Co_3O_4 which is also expressed by its voltammograms. The specific capacitance of the Co_3O_4 supercapacitor reduced from 476 F g^{-1} to 150 F g^{-1} at progressively increasing current densities from 0.5 A g^{-1} to 2.5 A g^{-1}. The long term stability was investigated at current density 2.5 A g^{-1} as shown in Figure 7c. Inset figure shows the galvanostatic charge−discharge cycles. Co_3O_4 hexagonal platelets cell exhibited an increase in specific capacitance during the initial cycles corresponds to the activation process[49] followed by more than 82% capacitance retention in next 2000 cycles, which demonstrate high cycling stability.

Figure 7d represents the Ragone plot of the Co_3O_4 supercapacitor. The energy density and the power density were calculated using formulas discussed in the Experimental Section. The Co_3O_4 two electrode cell delivered an energy density and power density of 42.3 Wh kg^{-1} and 1.56 kW kg^{-1}, respectively, at current density of 0.5 Ag^{-1}. The cell still maintains an energy density of 4.92 Wh kg^{-1} with power density as high as 6.4 kW kg^{-1} at a current density of 10 Ag^{-1}. These results show that Co_3O_4 hexagonal platelets have large pseudocapacitance, good reversibility, and excellent cycling stability, which may have potential applications in super-capacitors.

4. CONCLUSIONS

Highly stable, 0D and 2D cubic spinel structure Co_3O_4 nanospheres and hexagonal platelets have been synthesized from $Co(CH_3COO)_2.4H_2O$ precursor in ethanol solvent following a simple solvothermal condition. The change in the morphology from 0D to 2D is reaction time dependent. Structural characterization shows extremely good quality nanocrystals formation. The optical absorbance measurements show two clear absorption peaks and hence two optical band gaps of Co_3O_4 nanoparticles. The electrochemical studies suggest that the Co_3O_4 hexagonal platelet is a better capacitive material and the platelet type of morphology making the most of the material accessible for electrolytic ions (K^+) and therefore a high capacitance is achieved. This can be further enhanced if a large surface area support or conductive filler is used with Co_3O_4 nanocrystals.

■ ASSOCIATED CONTENT

Ⓢ Supporting Information

Table on various control syntheses, their XRDs and TEM images; BET data of cubic CoO. Additional TEM images of as-synthesized β-$Co(OH)_2$, expanded XRD; CV of hexagonal β-$Co(OH)_2$, annealed spherical Co_3O_4, and cubic CoO nano-particles; Nyquist plot of Co_3O_4 cell. This material is available free of charge via the Internet at http://pubs.acs.org.

■ AUTHOR INFORMATION

Corresponding Author

*E-mail: sdeka@chemistry.du.ac.in.

Author Contributions

‡Authors K.D. and S.K.U. contributed equally

Notes

The authors declare no competing financial interest.

■ REFERENCES

(1) He, T.; Chen, D.; Jiao, X. *Chem. Mater.* **2004**, *16*, 737−743.

(2) Liang, H.; Raitano, J. M.; Zhang, L.; Chan, S.-W. *Chem. Commun.* **2009**, *2009*, 7569−7571.

(3) Wang, H.; Zhang, L.; Tan, X.; Holt, C. M. B.; Zahiri, B.; Olsen, B. C.; Mitlin, D. *J. Phys. Chem. C* **2011**, *115*, 17599−17605.

(4) Meher, S. K.; Rao, G. R. *J. Phys. Chem. C* **2011**, *115*, 15646−15654.

(5) Wang, X.; Sumboja, A.; Khoo, E.; Yan, C.; Lee, P. S. *J. Phys. Chem. C* **2012**, *116*, 4930−4935.

(6) Cao, A.-M.; Hu, J.-S.; Liang, H.-P.; Song, W.-G.; Wan, L.-J.; He, X.-L.; Gao, X.-G.; Xia, S.-H. *J. Phys. Chem. B* **2006**, *110*, 15858−15863.

(7) Na, C. W.; Woo, H.-S.; Kim, I. D.; Lee, J.-H. *Chem. Commun.* **2011**, *47*, 5148−5150.

(8) Patil, D.; Patil, P.; Subramanian, V.; Joy, P. A.; Potdar, H. S. *Talanta* **2010**, *81*, 37−43.

(9) Jia, C.-J.; Schwickardi, M.; Weidenthaler, C.; Schmidt, W.; Korhonen, S.; Weckhuysen, B. M.; Schuth, F. *J. Am. Chem. Soc.* **2011**, *133*, 11279−11288.

(10) Gasparotto, A.; Barreca, D.; Bekermann, D.; Devi, A.; Fischer, R. A.; Fornasiero, P.; Gombac, V.; Lebedev, O. I.; Maccato, C.; Montini, T.; Tendeloo, G. V.; Tondello, E. *J. Am. Chem. Soc.* **2011**, *133*, 19362−19365.

(11) Zhang, Z.; Geng, H.; Zheng, L.; Du, B. *J. Alloys Com.* **2005**, *392*, 317−321.

(12) Hu, L.; Peng, Q.; Li, Y. *J. Am. Chem. Soc.* **2008**, *130*, 16136−16137.

(13) Ma, C. Y.; Mu, Z.; Li, J. J.; Jin, Y. G.; Cheng, J.; Lu, G. Q.; Hao, Z. P.; Qiao, S. Z. *J. Am. Chem. Soc.* **2010**, *132*, 2608−2613.

(14) Li, Y.; Tan, B.; Wu, Y. *J. Am. Chem. Soc.* **2006**, *128*, 14258−14259.

(15) Verelst, M.; Ely, T. O.; Amiens, C.; Snoeck, E.; Lecante, P.; Mosset, A.; Respaud, M.; Broto, J. M.; Chaudret, B. *Chem. Mater.* **1999**, *11*, 2702−2708.

(16) Liu, X.; Qiu, G.; Li, X. *Nanotechnology* **2005**, *16*, 3035−3040.

(17) Yan, N.; Hu, L.; Li, Y.; Wang, Y.; Zhong, H.; Hu, X.; Kong, X.; Chen, Q. *J. Phys. Chem. C* **2012**, *116*, 7227−7235.

(18) Wang, D.; Wang, Q.; Wang, T. *Inorg. Chem.* **2011**, *50*, 6482−6492.

(19) Nam, K. M.; Shim, J. H.; Han, D.-W.; Kwon, H. S.; Kang, Y.-M.; Li, Y.; Song, H.; Seo, W. S.; Park, J. T. *Chem. Mater.* **2010**, *22*, 4446−4454.

(20) Li, H. B.; Yu, M. H.; Wang, F. X.; Liu, P.; Liang, Y.; Xiao, J.; Wang, C. X.; Tong, Y. X.; Yang, G. W. *Nature Commun.* **2013**, in press, DOI:10.1038/ncomms2932 (last accessed on 09/20/2013).

(21) Chen, S.; Zhu, J.; Wang, X. *J. Phys. Chem. C* **2010**, *114*, 11829−11834.

(22) Wang, G. P.; Zhang, L.; Zhang, J. *J. Chem. Soc. Rev.* **2012**, *41*, 797−828.

(23) Chen, W.; Rakhi, R. B.; Hu, L. B.; Xie, X.; Cui, Y.; Alshareef, H. N. *Nano Lett.* **2011**, *11*, 5165−5172.

(24) Zhang, X.; Shi, W.; Zhu, J.; Kharistal, D. J.; Zhao, W.; Lalia, B. S.; Hng, H. H.; Yan, Q. *ACS Nano* **2011**, *5*, 2013−2019.

(25) Li, Q.; Liu, J.; Zou, J.; Chunder, A.; Chen, Y.; Zhai, L. *J. Power Sources* **2011**, *196*, 565−572.

(26) Huggins, R. A. *Solid State Ionics* **2000**, *134*, 179−195.

(27) Kotz, R.; Carlen, M. *Electrochim. Acta* **2000**, *45*, 2483−2498.

(28) Miller, J. R.; Simon, P. *Science* **2008**, *321*, 651−652.

(29) Shim, B. S.; Chen, W.; Doty, C.; Xu, C.; Kotov, N. A. *Nano Lett.* **2008**, *8*, 4151−4157.

(30) Wu, Z.-S.; Wang, D.-W.; Ren, W.; Zhao, J.; Zhou, G.; Li, F.; Cheng, H.-M. *Adv. Funct. Mater.* **2010**, *20*, 3595−3602.

(31) Simon, P.; Gogotsi, Y. *Nat. Mater.* **2008**, *7*, 845−854.

(32) Rakhi, R. B.; Chen, W.; Cha, D.; Alshareef, H. N. *Nano Lett.* **2012**, *12*, 2559−2567.

(33) Wu, J. B.; Lin, Y.; Xia, X. H.; Xu, J. Y.; Shi, Q. Y. *Electrochim. Acta* **2011**, *56*, 7163−7170.

(34) Wang, Y.; Zhong, Z.; Chen, Y.; Ng, C. T.; Lin, J. *Nano Res.* **2011**, *4*, 695−704.

(35) Yang, L.; Cheng, S.; Ding, Y.; Zhu, X.; Wang, Z. L.; Liu, M. *Nano Lett.* **2012**, *12*, 321−325.

(36) Zhang, F.; Yuan, C.; Lu, X.; Zhang, L.; Che, Q.; Zhang, X. *J. Power Sources* **2012**, *203*, 250−256.

(37) Wang, G.; Shen, X.; Horvat, J.; Wang, B.; Liu, H.; Wexler, D.; Yao, J. *J. Phys. Chem. C* **2009**, *113*, 4357−4361.

(38) Xia, X. H.; Tu, J. P.; Wang, X. L.; Gu, C. D.; Zhao, X. B. *Chem. Commun.* **2011**, *47*, 5786−5788.

(39) Zhu, T.; Chen, J. S.; Lou, X. W. *J. Mater. Chem.* **2010**, *20*, 7015−7020.

(40) Xie, L.; Li, K.; Sun, G.; Hu, Z.; Lv, C.; Wang, J.; Zhang, C. *J Solid State Electrochem* **2013**, *17*, 55−61.

(41) Wu, Q.; Xu, Y.; Yao, Z.; Liu, A.; Shi, G. *ACS Nano* **2010**, *4*, 1963−1970.

(42) Kraus, W.; Nolze, G. *Powder Cell for MS-Windows*; software is freely available from Collaborative Computational Project No. 14, http://www.ccp14.ac.uk/tutorial/powdcell/index.html, last accessed in January 2013.

(43) Barreca, D.; Massignan, C.; Daolio, S.; Fabrizio, M.; Piccirillo, C.; Armelao, L.; Tondello, E. *Chem. Mater.* **2001**, *13*, 588−593.

(44) Wang, X.; Chen, X.; Gao, L.; Zheng, H.; Zhang, Z.; Qian, Y. *J. Phys. Chem. B* **2004**, *108*, 16401−16404.

(45) Patil, P. S.; Kadam, L. D.; Lokhande, C. D. *Thin Solid Films* **1996**, *272*, 29−32.

(46) Meher, S. K.; Justin, P.; Rao, G. R. *Nanoscale* **2011**, *3*, 683−692.

(47) Zhang, G.-Q.; Zhao, Y.-Q.; Tao, F.; Li, H.-L. *J. Power Sources* **2006**, *161*, 723−729.

(48) Stoller, M. D.; Ruoff, R. S. *Energy Environ. Sci.* **2010**, *3*, 1294−1301.

(49) Jiang, H.; Ma, J.; Li, C. *Chem. Commun.* **2012**, *48*, 4465−4467.